

# LEARNING MESH MOTION TECHNIQUES WITH APPLICATION TO FLUID-STRUCTURE INTERACTION \*

JOHANNES HAUBNER<sup>†</sup>, OTTAR HELLAN<sup>‡</sup>, MARIUS ZEINHOFFER<sup>‡</sup>, AND MIROSLAV KUČHTA<sup>‡</sup>

**Abstract.** Mesh degeneration is a bottleneck for fluid-structure interaction (FSI) simulations and for shape optimization via the method of mappings. In both cases, an appropriate mesh motion technique is required. The choice is typically based on heuristics, e.g., the solution operators of partial differential equations (PDE), such as the Laplace or biharmonic equation. Especially the latter, which shows good numerical performance for large displacements, is expensive. Moreover, from a continuous perspective, choosing the mesh motion technique is to a certain extent arbitrary and has no influence on the physically relevant quantities. Therefore, we consider approaches inspired by machine learning. We present a hybrid PDE-NN approach, where the neural network (NN) serves as parameterization of a coefficient in a second order nonlinear PDE. We ensure existence of solutions for the nonlinear PDE by the choice of the neural network architecture. Moreover, we present an approach where a neural network corrects the harmonic extension such that the boundary displacement is not changed. In order to avoid technical difficulties in coupling finite element and machine learning software, we work with a splitting of the monolithic FSI system into three smaller subsystems. This allows to solve the mesh motion equation in a separate step. We assess the quality of the learned mesh motion technique by applying it to a FSI benchmark problem.

**Key words.** Fluid-structure interaction, neural networks, partial differential equations, hybrid PDE-NN, mesh moving techniques, data-driven approaches

**1. Introduction.** Following the past few decades' success of deep learning in fields such as image processing and speech recognition [21], researchers have turned their use to solving differential equations of scientific computing. In [33], it is proposed to solve forward and inverse PDEs by parameterizing the solution as a neural network and solving the non-convex optimization problem of minimizing the squared residual of the PDE's strong form, an approach called Physics-Informed Neural networks that has many variants [8]. Moreover models known as neural operators have been developed, that are trained to solve an entire class of PDEs at the same time, for instance the DeepONet [26] and the Fourier Neural Operator [22], in a paradigm known as operator learning. Another line of work is to use neural networks to accelerate parts of numerical algorithms that are driven by heuristics or parameter tuning. If a parameter in an algorithm affects its performance and must be tuned by hand, it can instead be chosen during runtime by a neural network with access to some performance indicator. For instance, in [4, 39] the authors use neural networks to respectively pick a stabilization parameter of a finite element scheme and to automate the selection of a parameter affecting how coarse problems are constructed in algebraic multigrid methods. In [6], the authors use a convolutional neural network to accurately detect and localize shocks, allowing more efficient shock capturing and avoiding parameter tuning. Automating the selection of parameters in algorithms can improve both the efficiency of the numerical algorithm itself and the scientific workflow, by allowing the user to spend time on other tasks. If a step in an algorithms is driven by heuristics, there is no obvious way of making the optimal choice and learning how to do this from data might be feasible. We take inspiration from operator learning and attempt to solve with machine learning techniques the problem of boundary deformation extension, a computational subproblem that is typically defined by the solution of heuristically chosen PDEs. We do this using two distinct approaches. First, we present an approach where a neural network parameterizes a PDE, the solution of which defines an extension operator. Secondly, we present an approach where a neural network defines a correction to a standard extension operator.

Extending boundary deformation onto the whole domain is a task that can be a crucial and limiting factor in applications. It appears in monolithic arbitrary Lagrangian-Eulerian (ALE) formulations of fluid-structure interaction (FSI) problems, e.g., [42, 37], and the method of mappings for partial differential equation (PDE) constrained shape optimization problems, e.g., [29, 30, 32]. The task can be stated as follows. Let  $\Omega \subset \mathbb{R}^d$ ,  $d \in \{2, 3\}$ , be a domain and  $\partial\Omega$  be its boundary. Given a boundary displacement  $g : \partial\Omega \rightarrow \mathbb{R}^d$ , one needs to apply an extension operator to find a deformation field  $u : \Omega \rightarrow \mathbb{R}^d$  such that  $u|_{\partial\Omega} = g$  and  $(\text{id} + u)(\Omega)$  is a well-defined (Lipschitz) domain. This imposes requirements on  $g$  and the extension operator. Among other things,  $\text{id} + u : \Omega \rightarrow (\text{id} + u)(\Omega)$  needs

\*Ottar Hellan and Miroslav Kuchta acknowledge support from the Research Council of Norway, grant 303362. Johannes Haubner and Marius Zeinhofer acknowledge support from the Research Council of Norway, grant 300305.

<sup>†</sup>Institute of Mathematics and Scientific Computing, University of Graz, Austria ([johannes.haubner@uni-graz.at](mailto:johannes.haubner@uni-graz.at))

<sup>‡</sup>Department of Numerical Analysis and Scientific Computing, Simula Research Laboratory, Oslo, Norway ([hellanottar@simula.no](mailto:hellanottar@simula.no), [mariusz@simula.no](mailto:mariusz@simula.no), [miroslav@simula.no](mailto:miroslav@simula.no))

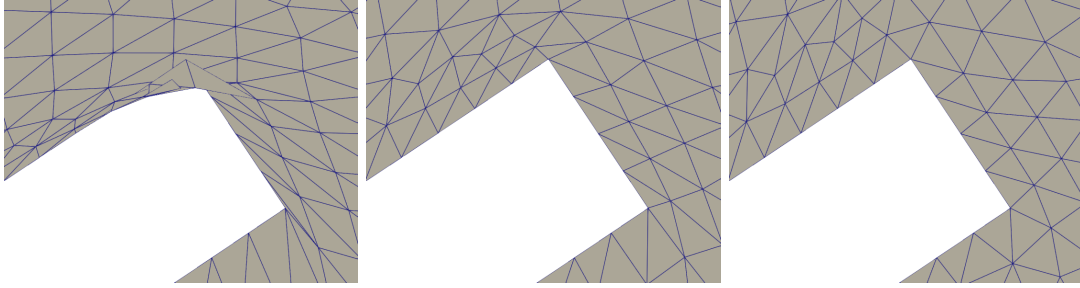


FIG. 1. Mesh degeneration at the top corner of the elastic structure for harmonic extension (left), but not for the learned extension operator (middle; here shown for hybrid PDE-NN approach with artificial training data) and biharmonic extension (right).

to be bijective, which also implies that  $g$  has to be chosen appropriately (e.g. not leading to a self-intersecting boundary of  $\Omega$ ). For computational purposes, it is mandatory that for any fixed mesh that discretizes  $\Omega$  the transformed mesh is non-degenerate, see Figure 1. The task of finding a suitable extension operator is typically based on heuristic choices, and has no (from a continuous perspective) or little (from a numerical perspective) influence on the physical solution as long as it is ensured that it fulfills the above described requirements. At the same time, it is the limiting factor for numerical simulations as soon as these requirements are violated. In this work, we apply ideas from machine learning to find a suitable extension operator for fluid-structure interaction problems formulated in the ALE framework.

Several approaches to define the extension operator have been introduced in the literature. In [42], harmonic extension operators, a linear elastic and a biharmonic model have been compared in the context of monolithic ALE formulations of FSI problems. The harmonic extension operator is obtained by solving the PDE

$$(1) \quad -\Delta u = 0 \quad \text{in } \Omega, \quad u = g \quad \text{on } \partial\Omega.$$

The linear elastic model is given by

$$-\text{div}(\eta_\lambda \text{tr}(\epsilon)I + 2\eta_\mu \epsilon) = 0 \quad \text{in } \Omega, \quad u = g \quad \text{on } \partial\Omega,$$

with  $\epsilon = \frac{1}{2}(\nabla u + \nabla u^\top)$  and scalar valued functions  $\eta_\lambda, \eta_\mu$  that are chosen, e.g., mesh dependent. In the context of shape optimization, [35] chooses  $\eta_\lambda = 0$  and  $\eta_\mu = \mu$ , where  $\mu$  solves the PDE

$$-\Delta \mu = 0 \quad \text{in } \Omega, \quad \mu = \mu_{\max} \quad \text{on } \Gamma, \quad \mu = \mu_{\min} \quad \text{on } \partial\Omega \setminus \Gamma,$$

for constants  $\mu_{\max}, \mu_{\min} > 0$ . The manually chosen boundary value allows to increase rigidity in areas where large deformations occur, e.g., around  $\partial\Omega$ . Finally, the biharmonic model given by

$$(2) \quad \Delta^2 u = 0 \quad \text{in } \Omega, \quad u = g, \quad \nabla u \cdot n = 0 \quad \text{on } \partial\Omega,$$

shows the best numerical behavior. However, it is the most expensive option since it requires either  $H^2$ -conforming finite elements, or other techniques such as a mixed approach, cf. e.g. [42, Sec. 4.4.5], or weakly imposed continuity of the normal derivatives [13]. Recently, in the context of shape optimization, also different types of extension equations were used. In contrast to fluid-structure interaction simulations, the choice of nonlinear extension operators is justified in many shape optimization applications since solving governing time-dependent PDEs for the state equation is the computational bottleneck of the shape optimization simulation. Differently from the fluid-structure interaction application, the choice of the extension operator can be part of the modeling and, e.g., used to define a shape metric based on the corresponding Steklov-Poincaré operator [36]. In [29], the  $p$ -Laplacian for  $p \geq 2$  was introduced as an extension equation. For  $1 < p < \infty$ , the problem is given by

$$-\text{div}(\|\nabla u\|^{p-2} \nabla u) = 0 \quad \text{in } \Omega, \quad u = g \quad \text{on } \partial\Omega,$$

where  $\|\cdot\|$  denotes the Frobenius norm. The nonlinearity increases the rigidity for increasing deformation gradient.

As a first approach to learn an extension operator, we consider a hybrid PDE-NN model [28]. We observe that the harmonic extension operator and the  $p$ -Laplacian are special cases of the more general formulation

$$(3) \quad -\operatorname{div}(\bar{\alpha}(\theta, \xi, u, \nabla u)\nabla u) = 0 \quad \text{in } \Omega, \quad u = g \quad \text{on } \partial\Omega,$$

where  $\bar{\alpha}$  is a scalar valued function,  $\xi$  denotes the coordinates and  $\theta$  parameters (e.g.,  $\theta = p$ ,  $\theta = \mu$ ). Here we shall parameterize  $\bar{\alpha}$  by using a neural network and in turn  $\theta$  represents the network’s weights and biases. The choice of  $\bar{\alpha}$  is made based on theoretical considerations such that existence of solutions of (3) is ensured. This requires a sophisticated choice of the architecture and the weights. In the scope of the work, for the sake of simplicity, we restrict ourselves to  $\bar{\alpha}(\theta, \xi, u, \nabla u) = \alpha(\theta, \|\nabla u\|^2)$ . We make a theoretically funded choice for the neural net, which serves as parameterization for  $\bar{\alpha}$ , such that existence of solutions of (3) is ensured. The choice of  $\bar{\alpha}$  then allows us to prove well-posedness of the extension operator by applying ideas from the proof that the  $p$ -Laplace equations have unique solutions. Moreover, we follow a supervised learning approach that aims to find a neural network such that the solution of (3) is close to the solution of the biharmonic extension. The resulting extension equation requires a nonlinear PDE solve. In order to make it suitable in the setting of the unsteady FSI equations, we follow a “lagging nonlinearity” approach, i.e. we consider the linear extension equation  $-\operatorname{div}(\bar{\alpha}(\theta, \xi, \bar{u}, \nabla \bar{u})\nabla u) = 0$  with  $\bar{u}$  being the deformation variable of the previous time-step in order to compute the new deformation field.

Our second approach is to learn an extension operator where a neural network corrects the harmonic extension operator. The choice of network architecture ensures that the resulting extension operator will always respect the boundary condition constraints, differing from other approaches where such constraints are penalized in the loss function. This is done by including in the network architecture multiplication of the output by a function vanishing on the boundary, which is found by solving a Poisson problem on the computational domain  $\Omega$ . Also here we follow a supervised learning approach, training the corrected harmonic extension operator to match the biharmonic extension operator.

In the hybrid PDE-NN approach we generalize the harmonic extension to a class of extensions and then select one of them by training a neural network. In the corrected harmonic extension approach, we instead use the harmonic extension as a base that is improved by a trained correction. Both approaches incorporate prior knowledge in the design of the neural networks, e.g. via respecting theoretical requirements or sophisticated choice of features. This is a common strategy. Features like periodicity, can be guaranteed in the network architectures by using a feature transformation, see e.g. [45]. Theoretical considerations and classical discretization schemes can be used as prior knowledge and be respected in the NN architecture. The choice in [34] is, e.g., based on theory of unsteady partial differential equations. On unstructured meshes, the connection between message-passing neural networks and classical discretization schemes is demonstrated in [23]. Physics-informed neural networks [33] incorporate knowledge or modeling assumptions on the physical model in the objective function. The hybrid PDE-NN approach proposed in [19, 44, 28] can itself be viewed as a (non-standard) neural network approach that learns a solution operator  $g \mapsto u$  of (3) from data and involves a solve of a partial differential equation in the output layer, which makes evaluations expensive compared to standard neural network architectures. Learning partial differential equations from data is also addressed e.g. in [1, 9, 10].

To assess the quality of the learned extension operator, we apply it to the FSI benchmark II [41]. More precisely, we do a comparison similar to [42, Fig. 6]. In order to be able to include different extension operators and assess their quality without having to modify the FSI system, we introduce a novel splitting scheme for the monolithic system. We discuss the hybrid PDE-NN approach in section 2. In section 3 we introduce the approach of correcting standard extension operators with a neural network. Section 4 presents the novel FSI splitting scheme and numerical results for the FSI benchmark II.

**2. Hybrid NN-PDE Approach.** In order to find the extension operator via (3), we formulate an optimization problem to find  $\bar{\alpha}$ :

Given boundary displacements  $g^i, i \in \{1, \dots, N_d\}, N_d \in \mathbb{N}$ , we search for weights  $\theta$  such that

$$(4) \quad \begin{aligned} & \min_{\theta \in \Theta, u \in W} \frac{1}{N_d} \sum_{i=1}^{N_d} \|u^i - u_{\text{biharm}}^i\|^2 + \lambda \mathcal{R}(\theta) \\ \text{s.t.} \quad & -\operatorname{div}(\bar{\alpha}(\theta, \xi, u^i, \nabla u^i)(\nabla u^i)) = 0 \quad \text{in } \Omega, \\ & u^i = g^i \quad \text{on } \partial\Omega, \end{aligned}$$

where  $\lambda > 0$  denotes a regularization parameter,  $\mathcal{R}(\theta)$  a regularization term,  $\Theta$  and  $W$  closed subsets of suitable Banach spaces, and  $\|\cdot\|$  is defined by

$$(5) \quad \|\cdot\|^2 = \|\cdot\|_{L^2(\Omega)}^2 + \|\nabla \cdot\|_{L^2(\Omega)}^2.$$

Moreover,  $u_{\text{biharm}}^i = u_{\text{biharm}}^i(g^i)$  solves the biharmonic equation for boundary conditions  $g = g^i$ . In order for the optimization problem to be well-defined, we have to choose  $\bar{\alpha}$  in a way such that the PDE constraint in (4) is solvable for all admissible  $\theta \in \Theta$ . This requires a suitable choice of  $\Theta$  and  $\bar{\alpha}$ , which we address in section 2.2. We model  $\bar{\alpha}$  via a neural net. Hence, we are in the setting of hybrid PDE-NN models [28].

**2.1. Choice of  $\bar{\alpha}$ .** The partial differential equation (3) is not necessarily solvable if we choose  $\bar{\alpha}(\theta, \xi, u, \nabla u)$  arbitrarily. In order to find conditions for  $\bar{\alpha}$  under which (3) can be ensured to be uniquely solvable, we take inspiration from the  $p$ -Laplace equations. The weak formulation of the  $p$ -Laplace equations,  $p > 1$ , can be viewed as the optimality conditions of the optimization problem

$$(6) \quad \min_{u \in W} \int_{\Omega} \|\nabla u\|^p d\xi.$$

Since (6) is a convex optimization problem with strictly convex objective, (6) has a unique solution. More precisely, we have the following result.

LEMMA 1 (see [24, Thm. 2.16]). *Let  $\Omega$  be a bounded Lipschitz domain,  $p \geq 2$ ,  $g \in W^{1,p}(\Omega)$ . Moreover, let*

$$W = \{u \in W^{1,p}(\Omega) : u|_{\partial\Omega} = g|_{\partial\Omega}\}.$$

*Then, there exists a unique minimizer of the optimization problem (6) and the solution of the optimization problem is characterized by*

$$(\|\nabla u\|^{p-2} \nabla u, \nabla \eta)_{L^2(\Omega)} = 0 \quad \forall \eta \in W_0^{1,p}(\Omega).$$

We prove a similar result for a more general class of PDEs. Hence, we consider a mapping  $\Lambda : \mathbb{R} \rightarrow \mathbb{R}$  and the optimization problem

$$(7) \quad \min_{u \in W} \int_{\Omega} \Lambda(\|\nabla u\|^2) d\xi$$

and work with

$$(8) \quad \alpha(\|\nabla u\|^2) = 2\Lambda'(\|\nabla u\|^2).$$

LEMMA 2. *Let  $\Omega$  be a bounded Lipschitz domain and  $g, W$  be defined as in lemma 1. Let  $\Lambda : \mathbb{R} \rightarrow \mathbb{R}$  be such that*

- $\Lambda$  is convex,
- $\Lambda$  is strictly increasing,
- $\Lambda$  is continuously differentiable,
- there exist  $a, b, d > 0, c \in \mathbb{R}$  and  $p > 2$  (or  $p = 2$  and  $\Lambda$  being affine) such that

$$(9) \quad |\Lambda(t)| \leq a + bt^{\frac{p}{2}},$$

and

$$(10) \quad |\Lambda'(t)| \leq c + dt^{\frac{p}{p-2}},$$

and  $\alpha$  be defined by (8). Then the mapping

$$(11) \quad F : W \rightarrow \mathbb{R}, \quad u \mapsto \int_{\Omega} \Lambda(\|\nabla u\|^2) d\xi,$$

is convex, continuous and Fréchet differentiable with derivative

$$(12) \quad F'(u) : W_0^{1,p}(\Omega) \rightarrow \mathbb{R}, \quad h_u \mapsto \int_{\Omega} \alpha(\|\nabla u\|^2) (\nabla u : \nabla h_u) d\xi.$$

*Proof.* In order to show continuity and differentiability of  $F$ , we rewrite

$$F(u) = f_3 \circ f_2 \circ f_1(u),$$

where

$$(13) \quad \begin{aligned} f_1 : & \quad W^{1,p}(\Omega)^d \rightarrow L^p(\Omega)^{d \times d}, \quad v \mapsto \nabla v, \\ f_2 : & \quad L^p(\Omega)^{d \times d} \rightarrow L^{\frac{p}{2}}(\Omega), \quad B \mapsto \|B\|^2, \\ f_3 : & \quad L^{\frac{p}{2}}(\Omega) \rightarrow \mathbb{R}, \quad \beta \mapsto \int_{\Omega} \Lambda(\beta) d\xi. \end{aligned}$$

Since  $f_1$  is linear,  $f_2$  is strictly convex and  $\Lambda$  is strictly increasing,  $F$  is convex. Due to [40, Sec. 4.3.3] we know that the superposition operator  $f_2$  is continuous and continuously differentiable with derivative  $f_2'(B) : L^p(\Omega)^{d \times d} \rightarrow L^{\frac{p}{2}}(\Omega)$ ,  $h_B \mapsto 2(B : h_B)$ , where  $B : h_B := \sum_{i,j} B_{ij}(h_B)_{ij}$ . Due to (9) and (10), we further obtain continuity and differentiability of  $f_3$  with derivative  $f_3'(\beta) : L^{\frac{p}{2}}(\Omega) \rightarrow \mathbb{R}$ ,  $h_\beta \mapsto \int_{\Omega} \Lambda'(\beta) h_\beta d\xi$ . Due to linearity and boundedness,  $f_1$  is continuous and differentiable with  $f_1'(v) : W^{1,p}(\Omega)^d \rightarrow L^p(\Omega)^{d \times d}$ ,  $h_v \mapsto \nabla h_v$ . Hence, by applying the chainrule we obtain continuity and differentiability of  $F : W^{1,p}(\Omega)^d \rightarrow \mathbb{R}$  with derivative  $F'(v)(h_v) = \int_{\Omega} 2\Lambda'(\|\nabla v\|^2) (\nabla v : \nabla h_v) d\xi$ . Since  $W$  is a closed, affine linear subspace of  $W^{1,p}(\Omega)^d$ , this concludes the proof.  $\square$

LEMMA 3. *Let the prerequisites of lemma 2 be fulfilled. Assume further that there exist  $e, f > 0$ , such that*

$$(14) \quad |\Lambda(t)| \geq e + ft^{\frac{p}{2}}.$$

Moreover, let  $g \in W^{1,p}(\Omega)$  and

$$W = \{u \in W^{1,p}(\Omega) : u|_{\partial\Omega} = g|_{\partial\Omega}\}.$$

Then, there exists a unique minimizer of the optimization problem (6) and the solution of the optimization problem is characterized by

$$(15) \quad (\alpha(\|\nabla u\|^2) \nabla u, \nabla \eta)_{L^2(\Omega)} = 0 \quad \forall \eta \in W_0^{1,p}(\Omega).$$

*Proof.* The proof follows the line of argumentation of [24, Thm. 2.16]. Assume  $u_1, u_2 \in W$  are solutions of (7). Since  $\Lambda$  is convex and strictly increasing and  $\nabla u \mapsto \|\nabla u\|^2$  is strictly convex, we know that  $\nabla u \mapsto \Lambda(\|\nabla u\|^2)$  is strictly convex. Hence, we know that  $\nabla u_1 = \nabla u_2$ . Therefore,  $u_1 = u_2 + C$  for a constant  $C > 0$ . Due to  $(u_1 - u_2)|_{\partial\Omega} = 0$ ,  $C = 0$ . This shows uniqueness of minimizers for (7).

In the following, we show existence of solutions. By the continuity of  $F$  shown in lemma 2, we have

$$(16) \quad I_0 := \inf_{v \in W} \int_{\Omega} \Lambda(\|\nabla v\|^2) d\xi \leq \int_{\Omega} \Lambda(\|\nabla g\|^2) d\xi < \infty.$$

Therefore, we can choose a sequence  $(v_j)_{j \in \mathbb{N}} \subset W$  such that  $\int_{\Omega} \Lambda(\|\nabla v_j\|^2) d\xi < I_0 + \frac{1}{j}$  for all  $j \in \mathbb{N}$ . Due to (14), we know that  $\|\nabla v_j\|_{L^p(\Omega)}$  is bounded. Since, by the Poincaré inequality, there exists a constant  $C > 0$  such that  $\|w\|_{L^p(\Omega)} \leq C \|\nabla w\|_{L^p(\Omega)}$  for all  $w \in W_0^{1,p}(\Omega)$ , we know that  $\|v_j - g\|_{L^p(\Omega)} \leq C \|\nabla(v_j - g)\|_{L^p(\Omega)}$  for all  $j \in \mathbb{N}$ . This implies boundedness of the sequence  $(\|v_j\|_{W^{1,p}(\Omega)})_{j \in \mathbb{N}}$ . Hence, there exists a weakly convergent subsequence  $(v_j)_{j \in J \subset \mathbb{N}}$  and  $v \in W$  such that  $v_j \rightharpoonup v$  weakly in  $W^{1,p}(\Omega)$  for  $J \ni j \rightarrow \infty$ . Since, by lemma 2,  $F : W \rightarrow \mathbb{R}$  is convex and continuous, it is weakly lower semicontinuous. Therefore,  $F(v) \leq \liminf_{J \ni j \rightarrow \infty} F(v_j) = I_0$  and  $v$  is the unique minimizer of (7). The first order necessary optimality conditions for the unconstrained optimization problem then yield (15).  $\square$

**2.2. Choice of the neural network.** We do a slight abuse of notation and write  $\alpha(\theta, s)$  instead of  $\alpha(s)$ , as well as  $\Lambda(\theta, s)$  instead of  $\Lambda(s)$ , in order to stress that our choices of  $\alpha$  and  $\Lambda$  depend on the weights and biases  $\theta$  of a neural net. By the considerations of the previous section, we choose

$$\bar{\alpha}(\theta, \xi, u, \nabla u) = \alpha(\theta, \|\nabla u\|^2) = 2 \frac{d}{ds} \Lambda(\theta, \|\nabla u\|^2),$$

where  $\Lambda : \Theta \times \mathbb{R} \rightarrow \mathbb{R}$  fulfills the requirements of (15). More precisely, we work with

$$(17) \quad \alpha(\theta, s) := 1 + (s - \eta_1)_{+, \epsilon} \frac{d}{ds} \tilde{\Lambda}(\theta, s) + (s - \eta_2)_{+, \epsilon},$$

where  $\eta_1 > 0$ ,  $\eta_2 \gg \eta_1$ ,  $\epsilon > 0$ ,  $(\cdot)_{+, \epsilon}$  denotes a monotonically increasing, smooth approximation of the  $\max(\cdot, 0)$  function and  $\tilde{\Lambda}(\theta, s)$  denotes a continuously differentiable, monotonically increasing, nonnegative Input Output Convex Neural Network [3, 38] that fulfills  $\tilde{\Lambda}(\theta, s) = \mathcal{O}(s)$  for  $s \rightarrow \infty$ . The last summand is not realized in the numerics and only needed if the second summand is zero.

The reason why we choose this specific form of  $\alpha$  is due to the fact that we want to keep the linearity of the extension operator close to the identity.

The  $\Lambda$  associated to (17) fulfills the properties of lemma 3:

- Since  $s \mapsto \tilde{\Lambda}(\theta, s)$  is convex and the mappings  $s \mapsto (s - \eta_1)_{+, \epsilon}$  and  $s \mapsto (s - \eta_2)_{+, \epsilon}$  are monotonically increasing,  $\frac{d}{ds} \alpha(\theta, s)$  is non-negative and  $\Lambda$  is convex.
- Since  $s \rightarrow \tilde{\Lambda}(\theta, s)$  is monotonically increasing,  $\frac{d}{ds} \tilde{\Lambda}(\theta, s) \geq 0$ . Therefore,  $\alpha(\theta, s) \geq 1$  and  $\Lambda$  is strictly increasing.
- Continuous differentiability of  $\Lambda$  follows from  $\alpha$  being a composition of continuous functions.
- The lower and upper bound estimates (9), (10) and (14) hold for  $p = 4$ .

In order to fulfill the requirements we ensure that the weights of  $\tilde{\Lambda}$  are nonnegative (we realize this by using squared weights).

Let  $\sigma$  denote an activation function. The neural network  $\tilde{\Lambda}(\theta, s) = x_{k+1}$  is given by the recursion

$$(18) \quad \begin{aligned} x_{k+1} &= W_k x_k + b_k, \\ x_{\ell+1} &= \sigma(W_\ell x_\ell + b_\ell), \quad \text{for } \ell \in \{0, \dots, k-1\} \\ x_0 &= s, \end{aligned}$$

with weights  $((W_0, b_0), (W_1, b_1), \dots, (W_k, b_k))$ . This type of neural networks is known as a multilayer perceptron (MLP).

For the hybrid PDE-NN approach, in order to ensure the properties of Lemma 3 we choose

$$((W_0, b_0), (W_1, b_1), \dots, (W_k, b_k)) = \psi(\theta),$$

with  $\theta = ((W_0^\theta, b_0^\theta), (W_1^\theta, b_1^\theta), \dots, (W_k^\theta, b_k^\theta))$  and

$$\psi : ((W_0^\theta, b_0^\theta), (W_1^\theta, b_1^\theta), \dots, (W_k^\theta, b_k^\theta)) \mapsto ((s[W_0^\theta], b_0^\theta), (s[W_1^\theta], b_1^\theta), \dots, (s[W_k^\theta], b_k^\theta)),$$

where  $s : t \mapsto t^2$ , and we use the notation in [17] to denote by  $s[\cdot]$  the entrywise application of  $s$  to a matrix  $\cdot$ . We work with the differentiable activation function  $\sigma(x) = \ln(1 + e^x)$ , with its derivative, the sigmoid function,  $\sigma'(x) = \frac{e^x}{1+e^x} = \frac{1}{1+e^{-x}}$ . Moreover, since it is not present in the derivative of the network, we choose the bias in the output layer as  $b_k^\theta = 0$ , where  $k$  is the depth of the neural network. Its derivative is therefore given by  $\frac{d}{ds} \tilde{\Lambda}(\theta, s) = y_{k+1}$ , where

$$\begin{aligned} y_{k+1} &= W_k y_k, \\ (y_{\ell+1})_i &= \sum_j \sigma'(W_\ell x_\ell + b_\ell)_{i,j} (W_\ell)_{i,j} (y_\ell)_j, \quad \text{for } \ell \in \{0, \dots, k-1\}, \\ x_\ell &= \sigma(W_{\ell-1} x_{\ell-1} + b_{\ell-1}), \quad \text{for } \ell \in \{0, \dots, k-1\}, \\ x_0 &= s, \quad y_0 = 1. \end{aligned}$$

Hence, motivated by theoretical considerations, we work with a non-standard neural network architecture.



**2.3. Approximation Properties of Convex Input Output Neural Network Architectures.** We discuss approximation capabilities of a class of shallow, input-convex neural networks. We show that for onedimensional input the ansatz class guarantees both convexity and universal approximation which renders it a promising candidate for later numerical studies. The convexity is crucial to ensure the solvability of the PDE at every iteration, whereas the universality provides the guarantee of sufficient expressiveness.

LEMMA 4. *Let  $f \in C^0(\mathbb{R})$  be convex, coercive, piecewise affine linear with  $n \in \mathbb{N}$  linear regions. Then  $f$  can be written in the form*

$$(19) \quad f(x) = c + \sum_{i=1}^n a_i \text{ReLU}(w_i x + b_i),$$

for  $a_i \geq 0$  and  $w_i, b_i, c \in \mathbb{R}$ .

*Proof.* Follows via induction over the number of linear regions.  $\square$

LEMMA 5. *Let  $f \in C^0(\mathbb{R})$  be convex. Then  $f$  can be approximated by ReLU networks as specified in Lemma 4 uniformly on compacta. This means, for any compact subset  $K \subset \mathbb{R}$  and  $\varepsilon > 0$  there is a network  $n = n(f, K, \varepsilon) : \mathbb{R} \rightarrow \mathbb{R}$  of the form (19) such that*

$$\sup_{x \in K} |f(x) - n(x)| < \varepsilon/2.$$

*Proof.* Follows from Lemma 4 and uniform continuity of  $f$  on any compact set  $K \subset \mathbb{R}$ .  $\square$

REMARK 1. *For  $d \geq 2$ , shallow input convex neural networks of the form*

$$(20) \quad f_\theta(x) = \sum_{i=1}^N c_i \rho(\tilde{w}_i \cdot x + \tilde{b}_i),$$

where  $c_i \geq 0$  and  $\rho = \text{ReLU}$ , yield no universal approximation to convex functions, see section A. There are other ansatz classes for input convex neural networks that have better approximation properties, see e.g. [5].

**3. NN-corrected Harmonic Extension Approach.** In contrast to the approach of learning  $\bar{\alpha}$  in a non-linear PDE (3) defining an extension operator, we explore a more direct approach by learning a neural network that realizes additive correction to the harmonic extension operator. This neural network takes pointwise input features from the harmonic extension and produces a correction to deal with boundary deformations where the harmonic extension degenerates. Typical boundary extension operators are based on PDEs, so we choose to use the component values and first order derivatives as input features, along with spatial coordinate  $\xi$ . We define the neural network-corrected harmonic extension as

$$(21) \quad u(\xi) = u_{\text{harm}}(\xi) + l(\xi) \cdot \mathcal{N}_\theta(\xi, u_{\text{harm}}(\xi), \nabla u_{\text{harm}}(\xi)),$$

where  $u_{\text{harm}}$  solves (1) with boundary condition  $u = g$  and  $\mathcal{N}_\theta$  is a learned function with parameters  $\theta$ . The function  $l$  is zero on the boundary  $\partial\Omega$  and positive in the interior  $\Omega$ , such that (21) satisfies the boundary condition  $u|_{\partial\Omega} = g$  exactly and the neural network affects the extension in every point in the interior[27]. We define the learned extension in this way because even small deviations from the boundary conditions will make the solution inadmissible for the purpose of the problem.

We construct our neural network as a standard multi-layer perceptron, defined by the recursion (18) and  $\mathcal{N}_\theta(x) = x_{k+1}$  for a network with  $k$  hidden layers. We write  $\theta$  for the collection of weights  $W_\ell$  and biases  $b_\ell$ , the parameters of the network to be trained, and refer to the dimensionality of  $x_\ell$  as the width of the  $\ell$ -th layer. We choose the Rectified Linear Unit  $\text{ReLU}(x) = \max(0, x)$  as activation function.

We choose to base our extension on the harmonic extension, since it is a linear equation with fast, order optimal solvers available and is suitable for modest boundary deformations. It is therefore a good starting point for the correction, without being prohibitively expensive to compute. Moreover, for a fixed architecture, evaluating the learned neural network correction  $\mathcal{N}_\theta$  scales linearly with the number of mesh points in terms of runtime and thus the NN-corrected harmonic extension approach should scale well for larger meshes.

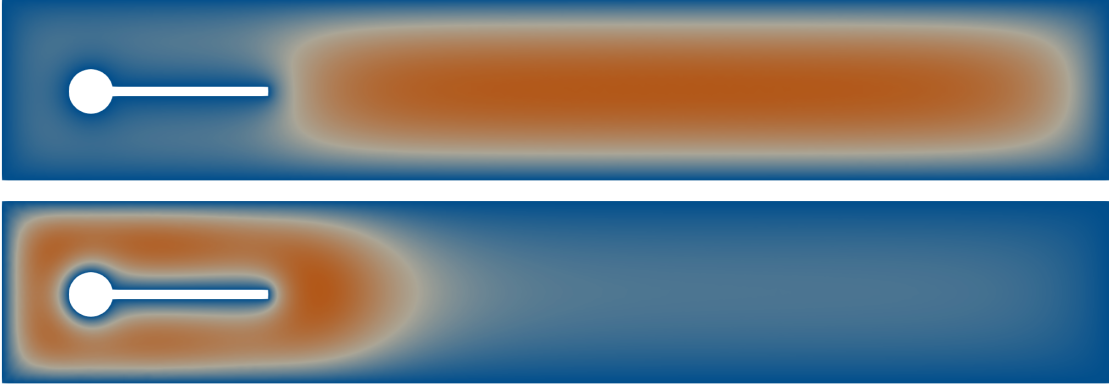


FIG. 2. Comparison of solutions to (22) with  $f = 1$  (top) and the hand-tuned  $f$  (23) (bottom).

We determine the function  $l$  as the solution of the Poisson problem

$$(22) \quad -\Delta l = f \text{ in } \Omega, \quad l = 0 \text{ on } \partial\Omega,$$

which for a wide class of  $f$  give solutions  $l$  that are strictly positive in the interior  $\Omega$  and smooth, see lemma 6. The option of  $f(\xi) \equiv 1$  is one choice of  $f$  such that this lemma holds.

LEMMA 6. *If  $f \in C^\infty(\Omega)$ , is bounded, non-negative and not identically zero,  $\Omega$  is bounded, and  $\partial\Omega$  is regular at every point, then there exists a unique classical solution  $l$  of (22), satisfying  $l \in C(\bar{\Omega}) \cap C^\infty(\Omega)$  and  $l(\xi) > 0$  for all  $\xi \in \Omega$ .*

*Proof.* By [14, Thm. 4.3], the Dirichlet problem (22) has a unique classical solution if every boundary point of  $\Omega$  is regular and  $f$  is bounded and locally Hölder continuous over  $\Omega$ . Thus, there exists a classical solution  $l$  of (22), which is by definition  $C^2(\Omega) \cap C(\bar{\Omega})$ . By the strong maximum principle, [14, Thm. 3.5], since  $\Delta l \leq 0$  in  $\Omega$  and  $l = 0$  on  $\partial\Omega$ ,  $l$  is positive in the interior. Since  $l$  is a classical solution of (22), it is also a weak solution in  $H^1(\Omega)$  and is  $C^\infty(\Omega)$  when  $f$  is  $C^\infty(\Omega)$ , [11, Sec. 6.3, Thm. 3].  $\square$

REMARK 2. *The domain in the FSI benchmark example is bounded by a finite number of simple closed curves, hence all boundary points are regular [14, p.26].*

The fact that  $l$  is strictly positive in the interior ensures that it is zero nowhere, so the neural network  $\mathcal{N}_\theta$  can correct the extension in all locations. The function  $l$  being smooth in the interior is not strictly necessary with our setup, but is an interesting fact that might be useful if higher differentiability of the total extension operator is desired. The values of  $l$  can also be normalized such that  $0 < l(\xi) < 1$  everywhere in  $\Omega$ , since by scaling  $f$  the solution of the linear PDE (22) will scale accordingly.

In our FSI test problem, we chose an  $f$  where  $l$  is normalized and  $l(\xi)$  is closer to 1 in the areas we know the harmonic extension is likely to degenerate and closer to 0 elsewhere. The choice of  $f$  was made by experimentation, adding terms until the resulting  $l$  solving (22) weighted the areas our prior knowledge told was important, ending up with an  $f$  proportional to

$$(23) \quad \tilde{f}(x, y) = 2(x + 1)(1 - x) \exp(-3.5x^7) + 0.1,$$

that we then normalized. Figure 2 shows the difference in  $l$  resulting from choosing  $f$  as (23) compared to using the simple  $f = 1$ .

Obtaining closed form solutions of (22) for arbitrary domains  $\Omega$  and source terms  $f$  is not possible, so the solution must be approximated using an appropriate discretization. Maximum principles do not necessarily translate into discrete ones, so since positivity of  $l$  in the interior is necessary, we selected continuous linear Lagrange ( $\mathbb{P}_1$ ) finite elements with a Delaunay triangulated mesh [18, Thm. 3.1], which satisfy a discrete maximum principle. We note that we only need to solve for  $l$  once for any given mesh and reuse the solution afterwards.

The neural network correction  $\mathcal{N}_\theta$  defines a  $d$ -dimensional vector field over the domain that we can evaluate where needed to solve the total computational problem. However, for the use in the FSI test problem it is convenient to embed the learned mesh displacement into a finite element function space. To this end, similar to the hybrid PDE-NN approach, we use the space of continuous piecewise



quadratic functions ( $\mathbb{P}_2$ ). For simplicity, the  $\mathbb{P}_2$  embedding of  $\mathcal{N}_\theta$  is obtained by linear interpolation (into midpoints) of its  $\mathbb{P}_1$  representation. In particular, this construction only requires evaluation of  $\mathcal{N}_\theta$  at mesh vertices.

In this work we restrict ourselves to neural networks operating on pointwise values, allowing the same network to be used for any triangulation of the domain, just by applying the network to each mesh point. We then need to encode sufficient information into the network to allow for correction of the mesh extension of varying boundary deformations. For example, predicting the extension correction using only the spatial coordinates  $\xi$  is not possible, since the network would not be able to distinguish the different boundary conditions  $u|_{\partial\Omega} = g$ . In addition to  $\xi$  we also include information from the already computed harmonic extension  $u_{\text{harm}}$ . To complement this (vertex-)local information the final network input is an approximate gradient  $u_{\text{harm}}$  at the vertex. We remark that since  $u_{\text{harm}}$  is represented by a  $C^0$ -conforming finite element function its gradient in a vertex cannot be simply obtained by standard nodal interpolation. Instead, we apply the Clément interpolation [7], which computes the approximation as the  $L^2$  projection over a patch composed by finite element cells connected to a given vertex. We note that the  $L^2$  approximation error of the recovered gradient (as  $\mathbb{P}_1$  function) decreases linearly with the mesh size [7]. Let us finally note that the local averaging gathers information from the neighboring vertices and is in this sense similar to aggregation in graph-neural networks [46]. In summary, the inputs to our neural network  $\mathcal{N}_\theta$  at  $\xi$  are  $(\xi, u_{\text{harm}}(\xi), D_c u_{\text{harm}}(\xi))$ , where  $D_c$  denotes approximating the Jacobian by Clément interpolation.

**4. FSI example.** In order to test the learned extension operators and compare them with respect to extension quality, we apply them to the FSI benchmark II. <sup>1</sup> We consider the coupling of the Navier-Stokes equations with St. Venant Kirchhoff type material and choose a monolithic ALE setting formulated on a fixed reference domain.

For the sake of convenience and brevity, we present the PDE system with a harmonic extension equation for the fluid displacement - other extension equations are more appropriate for large displacements and can be straightforwardly included into the system of equations [42, 15] as long as they can be represented as PDEs. The FSI model reads as follows.

$$(24) \quad \left. \begin{aligned} J\rho_f \partial_t v_f + J\rho_f ((F^{-1}(-\partial_t w_f)) \cdot \nabla) v_f - \operatorname{div}(J\sigma_f F^{-\top}) &= J\rho_f f & \text{on } \Omega_f \times (0, T), \\ \operatorname{div}(JF^{-1}v_f) &= 0 & \text{on } \Omega_f \times (0, T), \\ v_f &= v_{fD} & \text{on } \Gamma_f \times (0, T), \\ v_f(0) &= 0 & \text{on } \Omega_f, \\ \rho_s \partial_t v_s - \operatorname{div}(J\sigma_s F^{-\top}) &= \rho_s f_s & \text{on } \Omega_s \times (0, T), \\ \rho_s \partial_t w_s - \rho_s v_s &= 0 & \text{on } \Omega_s \times (0, T), \\ w_s(0) &= 0 & \text{on } \Omega_s, \\ v_s(0) &= 0 & \text{on } \Omega_s, \\ -\Delta w_f &= 0 & \text{on } \Omega_f \times (0, T), \\ w_f &= w_{fD} & \text{on } \Gamma_f \times (0, T), \\ \partial_t w_s &= v_s = v_f & \text{on } \Gamma_i \times (0, T), \\ -J\sigma_f F^{-\top} n_f &= J\sigma_s F^{-\top} n_s & \text{on } \Gamma_i \times (0, T), \\ w_f &= w_s & \text{on } \Gamma_i \times (0, T), \end{aligned} \right\}$$

where

$$\begin{aligned} \sigma_f(F) &= \rho_f \nu_f (Dv_f F^{-1} + F^{-\top} Dv_f^\top) - p_f \mathbf{I}, \\ F &= \mathbf{I} + Dw_s, \quad J(F) = \det(F), \quad E(F) = \frac{1}{2}(F^\top F - \mathbf{I}) \end{aligned}$$

and

$$\sigma_s(F) = J(F)^{-1} F (\mu_s (F^\top F - \mathbf{I}) + \lambda_s \operatorname{tr}(E(F)) \mathbf{I}) F^\top$$

<sup>1</sup>The code is available at <https://github.com/JohannesHaubner/LearnExt> for the hybrid PDE-NN approach and <https://github.com/ottarph/learnext-correction>, <https://github.com/ottarph/learnext-correction-FSI> for the NN-corrected harmonic approach.

for St. Venant Kirchhoff type material. Whenever it is clear from the context we write  $J$ ,  $E$ ,  $\sigma_f$ ,  $\sigma_s$  instead of  $J(F)$ ,  $E(F)$ ,  $\sigma_f(F)$ ,  $\sigma_s(F)$ .

$D \cdot$  denotes the Jacobian of function  $\cdot$ . We have compatibility conditions:  $v_{fD} = \partial_t w_{fD}$ ,  $v_{fD}(0) = 0$ . Let

$$\begin{aligned} V &\subset \{v \in H^1(\Omega)^d : v|_{\Gamma_f} = v_{fD}\}, \\ V_0 &\subset \{v \in H^1(\Omega)^d : v|_{\Gamma_f} = 0\}, \\ W &\subset \{v \in H^1(\Omega)^d : w|_{\Gamma_f} = w_{fD}\}, \\ W_0 &\subset \{v \in L^2(\Omega) : v|_{\Omega_f} \in H_0^1(\Omega_f)^d, v|_{\Omega_s} \in H^1(\Omega_s)^d\}, \\ P &\subset \{p \in L^2(\Omega_f) : \int_{\Omega_f} p d\xi = 0\}. \end{aligned}$$

The weak formulation is given by: Find  $(v, p, w) \in V \times P \times W$  such that

$$\begin{aligned} &\mathcal{A}(v, p, w)(\psi^v, \psi^p, \psi^w) \\ (25) \quad &= (J\rho_f \partial_t v, \psi^v)_{\Omega_f} + (J\rho_f ((F^{-1}(-\partial_t w)) \cdot \nabla)v, \psi^v)_{\Omega_f} + (J\sigma_f F^{-\top}, D\psi^v)_{\Omega_f} \\ &- (J\rho_f f, \psi^v)_{\Omega_f} + (\rho_s \partial_t v, \psi^v)_{\Omega_s} + (J\sigma_s F^{-\top}, D\psi^v)_{\Omega_s} + (\rho_s (\partial_t w - v), \psi^w)_{\Omega_s} \\ &+ \alpha_w (Dw, D\psi^w)_{\Omega_f} + (\operatorname{div}(JF^{-1}v), \psi^p)_{\Omega_f} = 0 \end{aligned}$$

for all  $(\psi^v, \psi^p, \psi^w) \in V_0 \times P \times W_0$ .

**4.1. Splitting the FSI problem into smaller subproblems.** In order to simplify the use of arbitrary extension operators, we propose a splitting scheme that handles the extension in a separate step. To do so, we build on ideas and techniques that are also present in, e.g., [12, 43]. The method proposed in [12] substitutes the condition  $\partial_t w_s = v_s$ , i.e.  $w_s(t + \Delta t) = w_s(t) + \int_t^{t+\Delta t} v_s(\xi) d\xi$ , into  $\sigma_s$ .

We motivate a similar procedure, use the reasoning of [12] to reduce the system but combine it with another idea. After transformation to the physical domain, the choice of  $w_f$  in the interior of  $\Omega_f$  does not affect the result of the fluid solution (as long as it is ensured that the corresponding transformation is bi-Lipschitz). Therefore, in the first step, we use  $w(t + \Delta t) = \tilde{w}(t) + \int_0^{\Delta t} v(t + s) ds$ , where  $\tilde{w}(t)$  denotes a deformation field at timepoint  $t$ . After having computed  $v(t + \Delta t)$  and  $p(t + \Delta t)$ , we compute  $w|_{\Omega_s}(t + \Delta t)$  and  $\tilde{w}(t + \Delta t)$  by applying an extension operator of the solid displacement onto the fluid domain. In this way, we solve for  $(v, p)$  and  $\tilde{w}$  separately without doing an approximation. Then, we need to recompute  $(v, p)$  for the modified deformation field  $\tilde{w}$  (which replaces  $w$  for the time-stepping). Thus, the procedure requires to solve the fluid system twice.

More precisely, assume we know the states  $\tilde{w}$ ,  $v$ ,  $p$  at the time step  $t$ . In order to get the states at time step  $t + \Delta t$  we have to solve three systems of equations. For the case of using an harmonic extension operator the procedure is given as follows.

**First system.** Let  $F(t + \delta t) = I + D(\tilde{w} + \int_t^{t+\delta t} v(\xi) d\xi)$ ,  $J = \det(F)$  and get  $v(t + \delta t)$ ,  $p(t + \delta t)$  for any  $\delta t > 0$  as the solution of

$$\begin{aligned} (26) \quad &(J\rho_f \partial_t v, \psi^v)_{\Omega_f} + (J\sigma_f F^{-\top}, D\psi^v)_{\Omega_f} \\ &- (J\rho_f f, \psi^v)_{\Omega_f} + (\rho_s \partial_t v, \psi^v)_{\Omega_s} + (J\sigma_s F^{-\top}, D\psi^v)_{\Omega_s} \\ &+ (\operatorname{div}(JF^{-1}v), \psi^p)_{\Omega_f} = 0, \end{aligned}$$

with  $\sigma_f = \sigma_f(F)$  and  $\sigma_s = \sigma_s(F)$ .

**Second system.** Given the solution of the first system we consider the solution of

$$(27) \quad (\rho_s (\partial_t w - v), \psi_s^w)_{\Omega_s} + \alpha_w (Dw, D\psi_f^w)_{\Omega_f} = 0,$$

where we impose the Dirichlet boundary conditions  $w|_{\partial\Omega_f} = (\tilde{w} + \int_t^{t+\delta t} v(\xi) d\xi)|_{\partial\Omega_f}$ . The solution of this system is used to update  $\tilde{w}$ . (Here, we use the subscripts  $\cdot_f$  and  $\cdot_s$  in order to clarify that these two equations are solved independently.) It is straightforward to replace the harmonic extension with an arbitrary extension operator that extends the boundary displacement to the interior of the domain, e.g., also those that are not defined via the solution of a PDE.

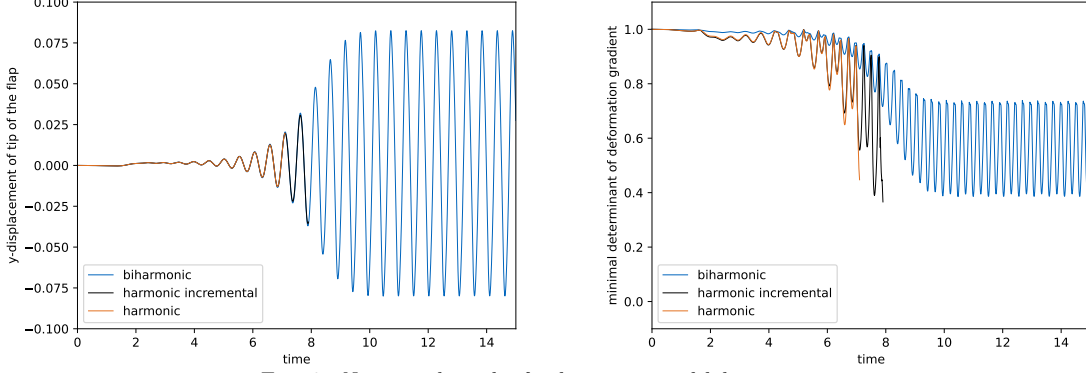


FIG. 3. Numerical results for harmonic and biharmonic extensions.

**Third system.** Given  $\tilde{w}$  we obtain the updated  $v, p$  as the solution of

$$\begin{aligned}
 (28) \quad & (J\rho_f\partial_tv, \psi^v)_{\Omega_f} + (J\rho_f((F^{-1}(v - \partial_tw)) \cdot \nabla)v, \psi^v)_{\Omega_f} + (J\sigma_f F^{-\top}, D\psi^v)_{\Omega_f} \\
 & - (J\rho_f f, \psi^v)_{\Omega_f} + (\rho_s\partial_tv, \psi^v)_{\Omega_s} + (J\sigma_s F^{-\top}, D\psi^v)_{\Omega_s} \\
 & + (\text{div}(JF^{-1}v), \psi^p)_{\Omega_f} = 0.
 \end{aligned}$$

where  $F = I + D(\tilde{w})$ ,  $J = \det(F)$ ,  $\sigma_f = \sigma_f(F)$  and  $\sigma_s = \sigma_s(F_s)$  with  $F_s(t + \delta t) = \tilde{w} + \int_t^{t+\delta t} v(\xi)d\xi$ .

**4.2. Discretization.** The discretization is done as in [42, 12, 15]. We choose the lowest-order Taylor-Hood finite elements for the velocity and pressure. The deformation is discretized using piecewise quadratic continuous finite elements. We further choose a shifted Crank-Nicolson scheme for performing the time-stepping. The pressure term and the incompressibility condition are handled implicitly. In the first summand of the weak form,  $J$  is replaced by a  $J_\theta$ , which is a convex combination of the determinant of the deformation gradient of the previous and current time step.

The time-step size is iteratively adapted. We choose a time-step-size range  $[\Delta t_{min}, \Delta t_{max}]$  and start with time-steps of size  $\Delta t = \Delta t_{max}$ . If the systems with the maximal time-step get unsolvable, we choose  $\Delta t = \max(\Delta t_{min}, \frac{1}{2}\Delta t)$ . This is repeated until we obtain solvability or reach  $\Delta t_{min}$ . If the system is not solvable for  $\Delta t = \Delta t_{min}$ , we stop. After each successful step we adapt the time-step by setting  $\Delta t = \min(2\Delta t, \Delta t_{max})$ .

**4.3. Numerical Results for FSI problem.** In order to validate the splitting of the FSI system in section 4.1, we apply it to the FSI benchmark II [41] and plot the displacement of the tip of the flap in Figure 3, compare e.g. [41, p. 256] or [15, Fig. 5.6]. We test the harmonic extension, the biharmonic extension and an incremental version of the harmonic extension where the extension is performed on the deformed domain of the previous timestep and only the change of the displacement is extended harmonically, see [37]. Moreover, Figure 3 shows the minimal determinant value of the deformation gradient. The simulations of the standard and incremental (see [37]) harmonic extension break if the deformation gradient for the next time-step is close to being non-invertible. Therefore, with these approaches, it is not possible to simulate the whole time interval.

#### 4.3.1. Generation of Training Data.

**Training data via FSI benchmark II.** For a proof of concept study, we first generate training data by running the FSI benchmark II with the biharmonic extension and a time-step size of 0.0025, and save the deformations for every time step in (15, 17] for the hybrid PDE-NN (and (11, 17] for the NN-corrected harmonic extension approach), i.e., we generate  $N_d = 800$  (and  $N_d = 2400$ , respectively) data points.

**REMARK 3.** *This procedure only makes sense if the FSI problem is solved several times as it is the case, e.g., if the FSI equations are the governing equations of a PDE constrained optimization problem. Moreover, since it is not necessary that the test data is physically realistic, the test set can also be artificially generated. Instead of solving the biharmonic equations and using this as a reference*



FIG. 4. The body deformations caused by the six base load configurations the artificial dataset is based on.

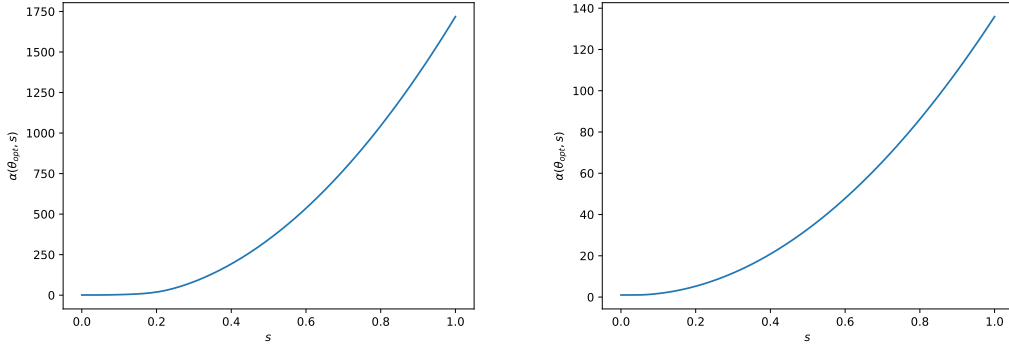


FIG. 5. Visualization of learned neural net  $\alpha(\theta, s)$  in the hybrid PDE-NN approach based on training data via FSI benchmark II (left) and artificial training data (right).

value, also unsupervised learning approaches

$$\begin{aligned} \min_{\theta \in \Theta, u \in W} \frac{1}{N_d} \sum_{i=1}^{N_d} \mathcal{J}(u^i) + \lambda \mathcal{R}(\theta) \\ \text{s.t. } u^i = \text{Ext}_{\theta}(g^i) \quad \text{for } i \in \{1, \dots, N_d\} \end{aligned}$$

can be considered, where  $\text{Ext}_{\theta}$  denotes an extension operator that depends on the parameters  $\theta$  and  $\mathcal{J}$  denotes a quality measure for the deformed mesh. For example, one can choose  $\mathcal{J}$  such that the determinant of the transformation gradient is bounded away from 0, see [16]. This, however, is left for future research. Alternatively, one can also work with artificial datasets.

**Artificial training data.** We also created an artificial dataset to train our networks on. This artificial dataset was created by solving for the stationary deformation of a neo-Hookean body representing the solid domain, with the same Lamé parameters as the solid in the FSI simulations. Specifically, we prescribe 0 displacement on the cylinder boundary and let the body deform under boundary loads selected by hand to create deformations of the solid domain resembling by eye features of the deformations encountered in the FSI benchmark II. Six different load configurations were selected and for each of these configurations 101 different deformations were computed, by varying the amplitude of the loads by the factor  $\cos(\theta)$  for 101 linearly spaced values of  $\theta$  from 0 to  $2\pi$ . These solid deformations were extended to the fluid domain by the harmonic and biharmonic extension, to serve as input data and target data respectively. In each base load configuration, there is one uniform boundary load acting on the entire right side of the body and one uniform boundary load acting uniformly and equally on a small region near the middle of the top and bottom of the body, this region varying in both length and center. The solid displacements corresponding to the six base load configurations are shown in Figure 4.

**4.3.2. Hybrid PDE-NN Approach.** In order to reduce the computational burden, we only take every  $\lfloor \frac{N_d}{N} \rfloor$ th training data point into account and work with  $N = 20$  for the FSI training data set and  $N = 60$  for the artificial data set. Every objective function evaluation requires the solution of  $N$  nonlinear PDEs (which could potentially be done fully parallel). In our numerical realization we do not use regularization, i.e., we work with  $\lambda = 0$ .

We choose  $\alpha$  to be a neural network with two hidden layers of dimension 5 with bias on the two hidden layers. Let  $\theta_{opt}$  denote the approximate solution of the optimization problem (4) that we obtain if we apply an L-BFGS method with at maximum 100 iterations. Figure 5 visualizes a neural network for  $\theta = \theta_{opt}$  that we obtained by training. In our numerical experiments  $\|\nabla u\|^2$  reaches values up to around 0.6 for the nonlinear learned extension operator applied to the FSI benchmark II.

We consider different strategies and show the numerical results in Figure 6 and Figure 7 where we choose  $\Delta t_{max} = 0.01$  and  $\Delta t_{min} = \frac{1}{128} \Delta t_{max}$ :

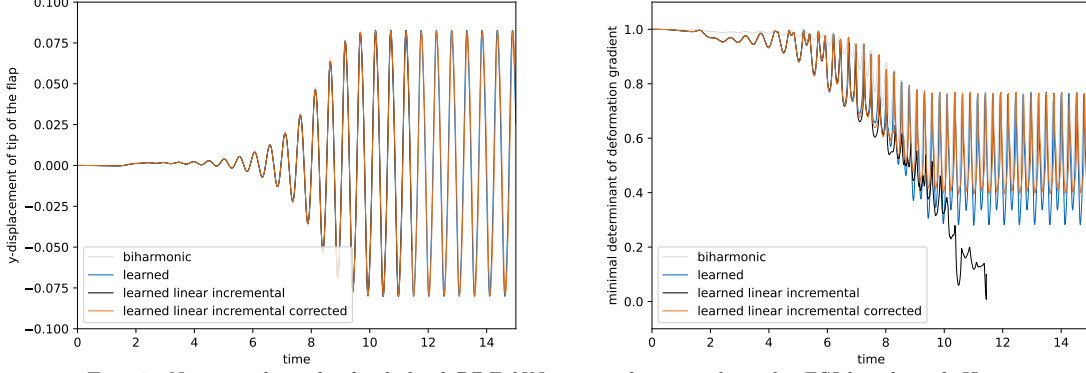


FIG. 6. Numerical results for hybrid PDE-NN approach, trained on the FSI benchmark II training set.

- **Strategy 1:** First we try the learned nonlinear extension operator, i.e., we solve (3) with  $\bar{\alpha}$  defined by (17) and  $\theta = \theta_{opt}$ . This strategy does not fail due to mesh degeneration. However, it requires several Newton-steps for large displacements.
- **Strategy 2:** In order to avoid the nonlinearity, we consider a strategy that uses a linear version of the extension operator. Working with a “lagging nonlinearity”, i.e., solving (3) with  $\bar{\alpha}$  defined by (17) being approximated by

$$(29) \quad \bar{\alpha}(\theta_{opt}, \xi, u, \nabla u) \approx \alpha(\theta_{opt}, \|\nabla u_{old}\|^2),$$

where  $u_{old}$  denotes the displacement of the previous time-step shows unsatisfactory numerical behaviour. Therefore, we combine it with the idea of using incremental versions for extension operators, see [37]. We present results for the incremental “lagging nonlinearity” strategy, where we solve

$$\begin{aligned} -\operatorname{div}(\alpha(\theta_{opt}, \|\nabla u_{old}\|^2) \nabla u_{\Delta}) &= 0 \quad \text{in } (\operatorname{id} + u_{old})(\Omega), \\ u_{\Delta} &= g - g_{old} \quad \text{on } \partial((\operatorname{id} + u_{old})(\Omega)), \end{aligned}$$

and use the update

$$u = u_{old} + u_{\Delta} \circ (\operatorname{id} + u_{old})^{-1}.$$

This strategy is successful even for the largest appearing displacements. However, the mesh quality decreases during the periodic oscillations and it is not possible to simulate the whole 15 seconds.

- **Strategy 3:** In order to counteract the decreasing mesh quality that occurs with the second strategy during the oscillations, we consider a third strategy that combines strategies 1 and 2. If the vertical displacement of the tip of the flap is below a certain threshold (we use 0.005), we work with strategy 1, otherwise we choose strategy 2. This approach allows to simulate the whole 15 seconds and the mesh quality stays stable during the oscillations. Moreover, the nonlinear extension equation of strategy 1 just needs to be evaluated for few time-steps and in a regime with small deformations at the tip.

**4.3.3. NN-corrected harmonic extension approach.** In the NN-corrected harmonic extension, we train the neural network using all 2400 snapshots in the FSI dataset. Since we only need to compute the neural network correction and do not need to solve a PDE for each training example, we can train using massively more data than in the hybrid PDE-NN approach. We set aside the last 400 snapshots as the test set and further split the remainder into 1800 snapshots for training and 200 for validation. The validation set is used in training to make decisions during training, such as when to reduce the learning rate. The test set is set aside until the networks are fully trained and used to evaluate their performance. Finally, the NN-corrected harmonic extension with the trained network is implemented as the mesh fluid mesh extension strategy in the FSI benchmark II simulation and its performance is analyzed. When training on the artificially constructed dataset, we also use all the generated snapshots, but here train-validate-test split is done randomly. We again evaluate the trained network by using it in the NN-corrected harmonic extension for the FSI benchmark II simulation.

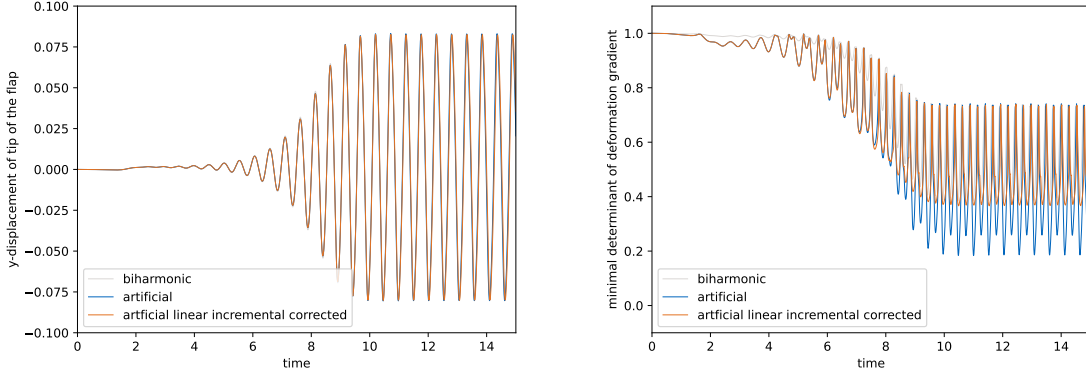


FIG. 7. Numerical results for hybrid PDE-NN approach, trained on the artificial training set.

We use a standard MLP for  $\mathcal{N}_\theta$  with 6 hidden layers of width 128 and ReLU activation function. The network has 8 input features, one for each component of  $\xi$ ,  $u_{\text{harm}}$ , and  $\nabla u_{\text{harm}}$ , and 2 output features, one for each component of the extension. Before the MLP, we include a normalization step, where inputs are normalized componentwise to have zero mean and unit variance over all mesh vertices and extension snapshots. These statistics are precomputed over the training set and are equal for all snapshots. The normalization layer uses statistics from the FSI dataset, both when trained on the FSI dataset and the synthetic dataset, as the FSI simulation is the test of main interest, and the statistics should be the same in both training and evaluation.

We implement the neural network  $\mathcal{N}_\theta$  using PyTorch[31]. The harmonic extension  $u_{\text{harm}}$  and boundary condition-preserving function  $l$  are computed using FEniCS[2], the FEM framework we use for the rest of our computations. The correction made by  $\mathcal{N}_\theta$  is translated into the finite element function spaces by adding the vertex evaluations of  $\mathcal{N}_\theta$  to the basis coefficient vectors.

We train our network in a supervised fashion by minimizing the discrete sum of absolute error in each mesh vertex for all snapshots, with the biharmonic extension as target. This can be formulated in the learning problem

$$(30) \quad \min_{\theta} \sum_i \sum_{\xi \in \mathcal{V}} \|u_{\text{harm}}^i(\xi) + l(\xi)\mathcal{N}_\theta(\xi, u_{\text{harm}}^i(\xi), D_c u_{\text{harm}}^i(\xi)) - u_{\text{biharm}}^i(\xi)\|_1,$$

where  $\mathcal{V}$  denotes the set of vertices in the computational mesh used to generate the dataset. We use the  $\|\cdot\|_1$ -norm instead of the more common  $\|\cdot\|_2^2$  because it tended to result in higher quality meshes.

To solve (30), we use the AdamW optimizer[25], a modification of the popular Adam optimizer[20] with improved efficiency when used with weight decay regularization. We used batching for different snapshots  $i$  and always include every vertex for each snapshot in the batch. We use a batch size of 128 snapshots during training, which is the largest power of 2 for which the entire batch fits on the GPU used. The network was trained for 500 epochs, with ReduceLRonPlateau learning rate scheduling, where the learning rate is reduced by a chosen factor when it stagnates. For this scheduler we used the default parameters, but with the reduction factor set to 0.5. We used weight decay regularization with factor 0.01 to reduce potential overfitting.

The neural network architecture was selected by experimenting with choosing different widths and depths until trained networks reduced the cost function well and the resulting extension was nicely behaved. We found that with the chosen architecture, the resulting extension varied quite smoothly over the domain, helping prevent small angles in elements, and the correction was mostly focused in the region of interest around the tip of the flap in the FSI test problem. We found that increasing either the depth or the width of the network increased its expressivity, i.e. ability to match the data, while increasing its depth made the networks vary more smoothly in space.

To predict the correction for a given harmonic extension  $u_{\text{harm}}$ , we must preprocess  $u_{\text{harm}}$  to supply the Clément interpolated gradients at each mesh vertex. For the training process, we did this beforehand and thereafter converted all the snapshots from FEniCS finite element functions to numpy-arrays that are easier to include in the PyTorch training process. When using the trained network as part of the simulation, this is done in each time step before the second step of the splitting method described in section 4.1. This interpolation is cheap when done repeatedly, as it can be realized by



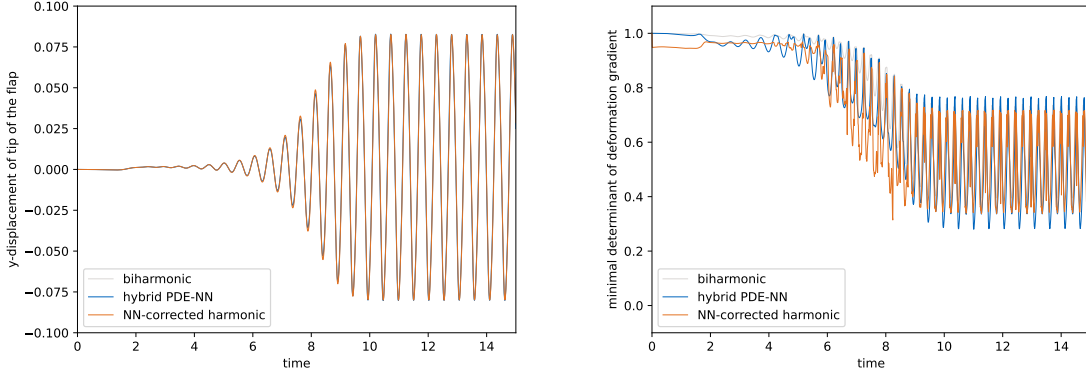


FIG. 8. Numerical results for the NN-corrected approach compared to the biharmonic and hybrid PDE-NN approaches, trained on the FSI benchmark II dataset.

multiplication with the same pre-assembled matrix for any given mesh.

To test the fully trained neural network correction (21), we evaluate it on the same FSI test problem as the hybrid PDE-NN approach. We solve the system (24) using the same splitting and discretization approach, outlined in sections 4.1-4.2. This deformation extension operator is not a PDE, but the splitting of the system allows us to use this extension, even though it does not naturally fit in the monolithic FSI formulation (24).

On the FSI test dataset, the fully trained network was able to produce a quality mesh for all snapshots, with the minimal determinant of deformation gradient being approximately 0.32 across all elements and snapshots. This is far from the degenerate case when this value approaches zero. When implemented as the mesh movement strategy in the FSI benchmark II simulation, the extension is successful and the simulation runs the whole 15 seconds period, as shown in Figure 8.

We also trained a neural network correction on the synthetic dataset, with the same architecture and training parameters as with the FSI-generated dataset. With the lower amount of training snapshots, we stopped the training process after only 200 epochs, as we found the training process had fully stabilized by then. We again used the FSI-generated test set for testing, as we wanted to train a network for the purpose of this FSI problem. We randomly split the synthetic dataset into 85% training data and 15% validation data. When evaluated on the test set, the fully trained network was able to produce a functional mesh for all snapshots, but not of high quality. On some snapshots, the resulting mesh was nearly degenerate, with minimal determinant of deformation gradient approximately 0.07. Still, the FSI simulation was able to run for the whole 15 second period when using this learned extension, as shown in Figure 9.

The reason the artificial dataset produces worse results than the FSI dataset could be that the artificial data is not similar enough to the data the network encounters in the FSI test problem. To support the argument, we analyzed the distribution of inputs to the neural network at different points around the flag from the synthetic dataset and the FSI dataset. Figure 10 shows a histogram of inputs at  $\xi = (0.6, 0.21)$ , the upper right corner of the flag, which is one of the points where the mesh degraded most. The missing tails in the neural network inputs at this point from the synthetic dataset indicate that there are characteristic deformations in the FSI simulation we did not reproduce.

The network was trained using an NVIDIA GeForce GTX 1660 SUPER and the process took approximately 16 minutes. Evaluating the network to produce an extension correction for every vertex of the mesh in the FSI simulations takes approximately 10 milliseconds per time step. The simulations run to produce the results in Figures 8-9 consisted of 2233 time steps, resulting in around 20 seconds spent on evaluating the neural network, although the real number is higher, since a portion of the time steps were rejected because the non-linear solver did not converge. In comparison, the total run time of the simulations was over 12 hours.

**5. Conclusion.** We presented two approaches to learn an operator that extends boundary deformation to the interior of the domain. We chose a supervised learning approach such that the operators approximate the solution of the biharmonic equation. We demonstrated that the learned operators have the potential to serve as mesh motion technique for FSI simulations. So far, we considered supervised learning approaches. For future work, e.g. in cases where the biharmonic extension does not

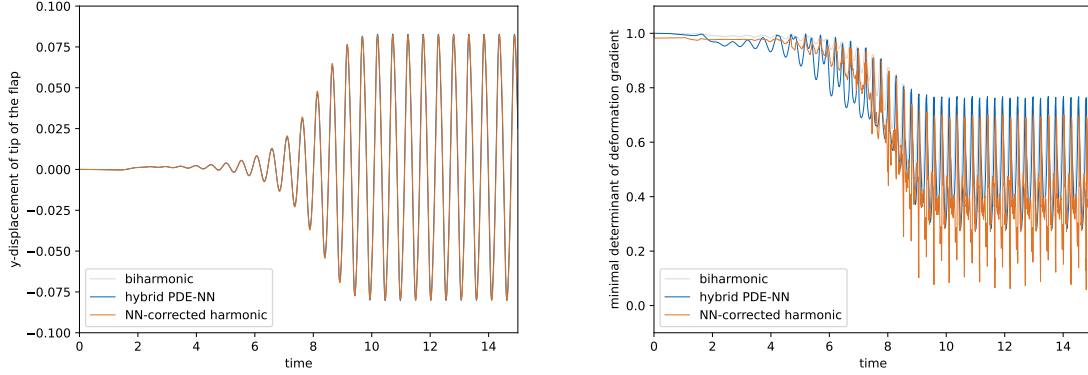


FIG. 9. Numerical results for the NN-corrected approach compared to the biharmonic and hybrid PDE-NN approaches, trained on the artificial dataset.

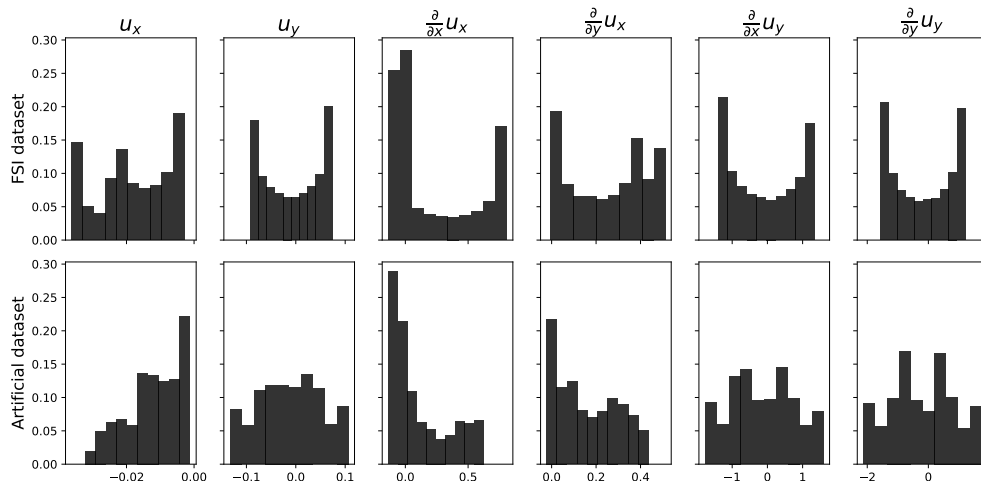


FIG. 10. Histogram of neural network inputs at upper right corner of the flag in artificial dataset. Parts of the distributions for the FSI dataset are not represented in the artificial dataset, indicating that there are features of the deformations in the FSI simulation that are not included in the artificial dataset.

give satisfactory results, it is also interesting to consider unsupervised approaches, where one tries to minimize a measure for the quality of the deformed mesh. Moreover, we worked with approaches that require the solution of a partial differential equation. Considering approaches that do not require PDE solves is another interesting direction for future research.

## REFERENCES

- [1] C. AARSET, M. HOLLER, AND T. T. N. NGUYEN, *Learning-informed parameter identification in nonlinear time-dependent PDEs*, 2022, <https://arxiv.org/abs/arXiv:2202.10915>.
- [2] M. ALNÆS, J. BLECHTA, J. HAKE, A. JOHANSSON, B. KEHLET, A. LOGG, C. RICHARDSON, J. RING, M. E. ROGNES, AND G. N. WELLS, *The FEniCS project version 1.5*, *Archive of Numerical Software*, 3 (2015).
- [3] B. AMOS, L. XU, AND J. Z. KOLTER, *Input convex neural networks*, in *International Conference on Machine Learning*, PMLR, 2017, pp. 146–155.
- [4] P. F. ANTONIETTI, M. CALDANA, AND L. DEDE', *Accelerating algebraic multigrid methods via artificial neural networks*, *Vietnam Journal of Mathematics*, 51 (2023), pp. 1–36, <https://doi.org/10.1007/s10013-022-00597-w>.
- [5] G. BALÁZS, A. GYÖRGY, AND C. SZEPESVÁRI, *Near-optimal max-affine estimators for convex regression*, in *Artificial Intelligence and Statistics*, PMLR, 2015, pp. 56–64.
- [6] A. D. BECK, J. ZEIFANG, A. SCHWARZ, AND D. G. FLAD, *A neural network based shock detection and localization approach for discontinuous Galerkin methods*, *Journal of Computational Physics*, 423 (2020), p. 109824, <https://doi.org/https://doi.org/10.1016/j.jcp.2020.109824>.
- [7] P. CLÉMENT, *Approximation by finite element functions using local regularization*, *Revue française d'automatique, informatique, recherche opérationnelle. Analyse numérique*, 9 (1975), pp. 77–84.
- [8] S. CUOMO, V. S. D. COLA, F. GIAMPAOLO, G. ROZZA, M. RAISSI, AND F. PICCIALLI, *Scientific machine learning through physics-informed neural networks: Where we are and what's next*, *Journal of Scientific Computing*, 92 (2022), <https://doi.org/10.1007/s10915-022-01939-z>.

- [9] G. DONG, M. HINTERMUELLER, AND K. PAPAITSOROS, *Optimization with learning-informed differential equation constraints and its applications*, 2020, <https://arxiv.org/abs/arXiv:2008.10893>.
- [10] G. DONG, M. HINTERMUELLER, K. PAPAITSOROS, AND K. VÖLKNER, *First-order conditions for the optimal control of learning-informed nonsmooth PDEs*, 2022, <https://arxiv.org/abs/arXiv:2206.00297>.
- [11] L. C. EVANS, *Partial differential equations*, no. v. 19 in Graduate studies in mathematics, American Mathematical Society, Providence, R.I., 2nd ed ed., 2010. OCLC: ocn465190110.
- [12] L. FAILER AND T. RICHTER, *A parallel Newton multigrid framework for monolithic fluid-structure interactions*, *Journal of Scientific Computing*, 82 (2020), pp. 1–27.
- [13] E. H. GEORGIOULIS AND P. HOUSTON, *Discontinuous Galerkin methods for the biharmonic problem*, *IMA journal of numerical analysis*, 29 (2009), pp. 573–594.
- [14] D. GILBARG AND N. S. TRUDINGER, *Elliptic partial differential equations of second order*, *Classics in mathematics*, Springer, Berlin ; New York, 2nd ed., rev. 3rd printing ed., 2001.
- [15] J. HAUBNER, *Shape Optimization for Fluid-Structure Interaction*, Dissertation, Technische Universität München, München, 2020.
- [16] J. HAUBNER, M. SIEBENBORN, AND M. ULBRICH, *A continuous perspective on shape optimization via domain transformations*, *SIAM Journal on Scientific Computing*, 43 (2021), pp. A1997–A2018, <https://doi.org/10.1137/20m1332050>.
- [17] F. HIAI, *Monotonicity for entrywise functions of matrices*, *Linear algebra and its applications*, 431 (2009), pp. 1125–1146.
- [18] W. HUANG, *Discrete maximum principle and a delaunay-type mesh condition for linear finite element approximations of two-dimensional anisotropic diffusion problems*, *Numerical Mathematics: Theory, Methods and Applications*, 4 (2011), pp. 319–334, <https://doi.org/10.4208/nmtma.2011.m1024>.
- [19] M. INNES, A. EDELMAN, K. FISCHER, C. RACKAUCKAS, E. SABA, V. B. SHAH, AND W. TEBBUTT, *A differentiable programming system to bridge machine learning and scientific computing*, arXiv preprint arXiv:1907.07587, (2019).
- [20] D. P. KINGMA AND J. BA, *Adam: A method for stochastic optimization*, 2017, <https://arxiv.org/abs/1412.6980>.
- [21] Y. LECUN, Y. BENGIO, AND G. HINTON, *Deep learning*, *Nature*, 521 (2015), pp. 436–444, <https://doi.org/10.1038/nature14539>.
- [22] Z. LI, N. KOVACHKI, K. AZIZZADENESHELI, B. LIU, K. BHATTACHARYA, A. STUART, AND A. ANANDKUMAR, *Fourier neural operator for parametric partial differential equations*, arXiv preprint arXiv:2010.08895, (2020).
- [23] M. LIENEN AND S. GÜNNEMANN, *Learning the dynamics of physical systems from sparse observations with finite element networks*, arXiv preprint arXiv:2203.08852, (2022).
- [24] P. LINDQVIST, *Notes on the p-laplace equation*, 2017.
- [25] I. LOSHCILOV AND F. HUTTER, *Decoupled weight decay regularization*, in *International Conference on Learning Representations*, 2017.
- [26] L. LU, P. JIN, G. PANG, Z. ZHANG, AND G. E. KARNIADAKIS, *Learning nonlinear operators via DeepONet based on the universal approximation theorem of operators*, *Nature Machine Intelligence*, 3 (2021), pp. 218–229, <https://doi.org/10.1038/s42256-021-00302-5>.
- [27] K. MCFALL AND J. MAHAN, *Artificial neural network method for solution of boundary value problems with exact satisfaction of arbitrary boundary conditions*, *IEEE Transactions on Neural Networks*, 20 (2009), pp. 1221–1233, <https://doi.org/10.1109/tnn.2009.2020735>.
- [28] S. K. MITUSCH, S. W. FUNKE, AND M. KUCHTA, *Hybrid FEM-NN models: Combining artificial neural networks with the finite element method*, *Journal of Computational Physics*, 446 (2021), p. 110651, <https://doi.org/10.1016/j.jcp.2021.110651>.
- [29] P. M. MÜLLER, N. KÜHL, M. SIEBENBORN, K. DECKELNICK, M. HINZE, AND T. RUNG, *A novel p-harmonic descent approach applied to fluid dynamic shape optimization*, arXiv preprint arXiv:2103.14735, (2021).
- [30] S. ONYSHKEVYCH AND M. SIEBENBORN, *Mesh quality preserving shape optimization using nonlinear extension operators*, *Journal of Optimization Theory and Applications*, 189 (2021), pp. 291–316.
- [31] A. PASZKE, S. GROSS, F. MASSA, A. LERER, J. BRADBURY, G. CHANAN, T. KILLEEN, Z. LIN, N. GIMELSHEIN, L. ANTIGA, A. DESMAISON, A. KÖPF, E. YANG, Z. DEVITO, M. RAISON, A. TEJANI, S. CHILAMKURTHY, B. STEINER, L. FANG, J. BAI, AND S. CHINTALA, *Pytorch: An imperative style, high-performance deep learning library*, 2019, <https://arxiv.org/abs/1912.01703>.
- [32] J. PINZON AND M. SIEBENBORN, *Fluid dynamic shape optimization using self-adapting nonlinear extension operators with multigrid preconditioners*, *Optimization and Engineering*, 24 (2023), pp. 1089–1113.
- [33] M. RAISSI, P. PERDIKARIS, AND G. E. KARNIADAKIS, *Physics-informed neural networks: A deep learning framework for solving forward and inverse problems involving nonlinear partial differential equations*, *Journal of Computational physics*, 378 (2019), pp. 686–707.
- [34] L. RUTHOTTO AND E. HABER, *Deep neural networks motivated by partial differential equations*, *Journal of Mathematical Imaging and Vision*, 62 (2020), pp. 352–364.
- [35] V. SCHULZ AND M. SIEBENBORN, *Computational comparison of surface metrics for PDE constrained shape optimization*, *Computational Methods in Applied Mathematics*, 16 (2016), pp. 485–496.
- [36] V. H. SCHULZ, M. SIEBENBORN, AND K. WELKER, *Efficient PDE constrained shape optimization based on Steklov–Poincaré-type metrics*, *SIAM Journal on Optimization*, 26 (2016), pp. 2800–2819, <https://doi.org/10.1137/15m1029369>.
- [37] A. SHAMANSKIY AND B. SIMEON, *Mesh moving techniques in fluid-structure interaction: robustness, accumulated distortion and computational efficiency*, *Computational Mechanics*, 67 (2020), pp. 583–600, <https://doi.org/10.1007/s00466-020-01950-x>.
- [38] S. SIVAPRASAD, A. SINGH, N. MANWANI, AND V. GANDHI, *The curious case of convex neural networks*, in *Joint European Conference on Machine Learning and Knowledge Discovery in Databases*, Springer, 2021, pp. 738–754.
- [39] T. TASSI, A. ZINGARO, AND L. DEDE, *A machine learning approach to enhance the SUPG stabilization method for*

*advection-dominated differential problems*, arXiv preprint arXiv:2111.00260, (2021).

- [40] F. TRÖLTZSCH, *Optimal Control of Partial Differential Equations*, American Mathematical Society, Apr. 2010, <https://doi.org/10.1090/gsm/112>.
- [41] S. TUREK AND J. HRON, *Proposal for numerical benchmarking of fluid-structure interaction between an elastic object and laminar incompressible flow*, in Fluid-structure interaction, Springer, 2006, pp. 371–385.
- [42] T. WICK, *Fluid-structure interactions using different mesh motion techniques*, Computers & Structures, 89 (2011), pp. 1456–1467.
- [43] J. XU AND K. YANG, *Well-posedness and robust preconditioners for discretized fluid–structure interaction systems*, Computer Methods in Applied Mechanics and Engineering, 100 (2015), pp. 69–91.
- [44] K. XU AND E. DARVE, *Adcme: Learning spatially-varying physical fields using deep neural networks*, 2020, <https://arxiv.org/abs/arXiv:2011.11955>.
- [45] A. YAZDANI, L. LU, M. RAISSI, AND G. E. KARNIADAKIS, *Systems biology informed deep learning for inferring parameters and hidden dynamics*, PLoS computational biology, 16 (2020), p. e1007575.
- [46] J. ZHOU, G. CUI, S. HU, Z. ZHANG, C. YANG, Z. LIU, L. WANG, C. LI, AND M. SUN, *Graph neural networks: A review of methods and applications*, AI Open, 1 (2020), pp. 57–81, <https://doi.org/https://doi.org/10.1016/j.aiopen.2021.01.001>.

## Appendix A. Counterexample.

We consider a shallow input convex neural network of the form

$$(31) \quad f_\theta(x) = \sum_{i=1}^N c_i \rho(\tilde{w}_i \cdot x + \tilde{b}_i),$$

where  $c_i \geq 0$ . If we work with  $\rho = \text{ReLU}$ ,  $f_\theta$  can be defined as

$$(32) \quad f_\theta(x) = \sum_{i=1}^N \rho(w_i \cdot x + b_i),$$

where  $w_i = c_i \tilde{w}_i$  and  $b_i = c_i \tilde{b}_i$ . While every convex function  $h : \mathbb{R} \rightarrow \mathbb{R}$  that is bounded from below can be approximated by a function of the form (32), this is not the case in general, e.g., not every convex function  $h : \mathbb{R}^2 \rightarrow \mathbb{R}$  that is bounded from below can be approximated.

In the following, we prove that we can not approximate the function

$$(33) \quad h : (x, y) \mapsto \max(\max(x + y, 0), \max(x - y, 0))$$

with a function of the form (32) (even for arbitrary large  $N$ ). We start by showing that the function  $h$  can not be represented exactly by (32). To do so, we use the following lemma.

LEMMA 7. *Let  $d \in \mathbb{N}$ ,  $N \in \mathbb{N}$ ,  $\{a_i, b_i\}_{i \in \{1, \dots, N\}}$  be such that  $a_i \in \mathbb{R}^d$ ,  $b_i \in \mathbb{R}$  for all  $i \in \{1, \dots, N\}$ . Let  $f(x) := \sum_{i=1}^N \rho(a_i^\top x + b_i)$  with  $\rho(s) = \text{ReLU}(s)$ . Let  $x_1, x_2 \in \mathbb{R}^d$  be such that  $f$  is differentiable at  $x_1$  and  $x_2$ , and  $\mathcal{A}(x_1) \cap \mathcal{A}(x_2) = \emptyset$ , where*

$$\mathcal{A}(x) = \{j \in \{1, \dots, N\} : a_j^\top x + b_j > 0\}.$$

Then,

$$(34) \quad \tilde{f}(x) := \sum_{j=1}^2 \rho(f'(x_j)^\top x + \sum_{i \in \mathcal{A}(x_j)} b_i)$$

fulfills  $f(x_j) = \tilde{f}(x_j)$  for  $j \in \{1, 2\}$  and

$$(35) \quad \tilde{f}(x) \leq f(x)$$

for all  $x \in \mathbb{R}^d$ .

*Proof.* Since  $f$  is assumed to be differentiable at  $x_j$ ,  $j \in \{1, 2\}$ ,

$$(36) \quad f'(x_j) = \sum_{i \in \mathcal{A}(x_j)} a_i.$$

For  $k \in \{1, 2\}$ , since  $\mathcal{A}(x_1) \cap \mathcal{A}(x_2) = \emptyset$ , we know that

$$\tilde{f}(x_k) = \sum_{j=1}^2 \rho\left(\sum_{i \in \mathcal{A}(x_j)} a_i^\top x_k + \sum_{i \in \mathcal{A}(x_j)} b_i\right) = \rho\left(\sum_{i \in \mathcal{A}(x_k)} (a_i^\top x_k + b_i)\right) = \sum_{i \in \mathcal{A}(x_k)} (a_i^\top x_k + b_i) = f(x_k).$$



FIG. 11. Contour plot of the function  $h$  (left) and a function  $f_\theta$  of the form (32) (right). This function is a lower bound for every function of the form (32) that is equal to  $h$  in  $[-k, 0] \times (-k, k)$ .

Moreover, since  $\rho(a+b) \leq \rho(a) + \rho(b)$  and  $\mathcal{A}(x_1) \cap \mathcal{A}(x_2) = \emptyset$ ,

$$\tilde{f}(x) = \sum_{j=1}^2 \rho\left(\sum_{i \in \mathcal{A}(x_j)} (a_i^\top x + b_i)\right) \leq \sum_{j=1}^2 \sum_{i \in \mathcal{A}(x_j)} \rho(a_i^\top x + b_i) \leq \sum_{i=1}^N \rho(a_i^\top x + b_i) = f(x)$$

for all  $x \in \mathbb{R}^d$ . □

**A.1. Exact representation.** We assume that there exists  $N \in \mathbb{N}$  and  $\{a_i, b_i\}_{i \in \{1, \dots, N\}}$  such that  $f_\theta(x) = h(x)$  for all  $x \in \mathbb{R}^d$ . We choose  $x_1 = (-\frac{k}{2}, \frac{3k}{4})^\top$  and  $x_2 = (-\frac{k}{2}, -\frac{3k}{4})^\top$  for  $k > 0$  sufficiently large. Since  $h(x) = 0$  for  $x \in (-\infty, 0) \times \{0\}$ , and  $h(x) = 0$  for  $x \in \{-\frac{k}{2}\} \times (-\frac{k}{2}, \frac{k}{2})$ , and  $f_\theta = h$ ,  $\mathcal{A}(x_1) \cap \mathcal{A}(x_2) = \emptyset$ . Moreover, differentiability of  $h$  at  $x_1$  and  $x_2$  gives

$$f'_\theta(x_1) = (1, 1)^\top, \quad f'_\theta(x_2) = (1, -1)^\top.$$

By lemma 7,

$$(37) \quad f_\theta(x) \geq \rho((1, 1)^\top x + \sum_{i \in \mathcal{A}(x_1)} b_i) + \rho((1, -1)^\top x + \sum_{i \in \mathcal{A}(x_2)} b_i).$$

For  $x = x_j$ ,  $j \in \{1, 2\}$ , we obtain  $f_\theta(x_j) = h(x_j) = \frac{k}{4}$ . Therefore, (37) gives for  $x \in \{x_1, x_2\}$ ,

$$\frac{k}{4} = \frac{k}{4} + \sum_{i \in \mathcal{A}(x_j)} b_i,$$

(where we used (36), the definition of  $\mathcal{A}$  and  $\mathcal{A}(x_1) \cap \mathcal{A}(x_2) = \emptyset$ .) and

$$\sum_{i \in \mathcal{A}(x_j)} b_i = 0.$$

Thus,

$$f_\theta(x) \geq \rho((1, 1)^\top x) + \rho((1, -1)^\top x).$$

Hence, for  $x = (\alpha, 0)^\top$ ,  $\alpha > 0$ , we obtain  $f_\theta((\alpha, 0)^\top) \geq 2\alpha$ . However,  $h((\alpha, 0)^\top) = \alpha$ . This yields a contradiction and implies that  $h(x)$  can not be represented by a function of the form (32).

**A.2. Approximation.** In the same fashion, we can also show that on the compact set  $K := [-k, k] \times [-k, k]$  there exists  $\epsilon > 0$  such that  $\sup_{x \in K} |f_\theta(x) - h(x)| > \epsilon$  for all  $f_\theta$  of the form (32).

We show it by contradiction. We assume that for every  $\epsilon > 0$  there exists a function  $f_{\theta, \epsilon}$  that fulfills

$$(38) \quad \sup_{x \in K} |f_{\theta, \epsilon}(x) - h(x)| \leq \epsilon$$

**A.2.1. Assumption on  $\mathcal{A}(x_1) \cap \mathcal{A}(x_2)$ .** We show that we can assume without loss of generality that  $f_{\theta, \epsilon}$  is such that  $\mathcal{A}(x_1) \cap \mathcal{A}(x_2) = \emptyset$ .

Since  $h(x) = 0$  for  $x \in (-\infty, 0) \times \{0\}$  and  $x \in \{-\frac{k}{2}\} \times (-\frac{k}{2}, \frac{k}{2})$ , and (38),

$$0 \leq \sum_{i \in \mathcal{A}(x_1) \cap \mathcal{A}(x_2)} \rho(a_i^\top x + b_i) \leq \epsilon$$

for all  $x \in (-\infty, 0) \times \{0\} \cup \{-\frac{k}{2}\} \times (-\frac{k}{2}, \frac{k}{2})$ . Let  $x_0 := (0, 0)^\top$  and  $x_3 := (-k, 0)^\top$ . We know (due to linearity of  $a_i^\top x + b_i$ ) that  $\mathcal{A}(x_1) \cap \mathcal{A}(x_2) = (\mathcal{A}(x_1) \cap \mathcal{A}(x_2) \cap \mathcal{A}(x_0)) \cup (\mathcal{A}(x_1) \cap \mathcal{A}(x_2) \cap \mathcal{A}(x_3)) \setminus (\mathcal{A}(x_1) \cap \mathcal{A}(x_2) \cap \mathcal{A}(x_0))$ . Hence,

$$(39) \quad \sum_{i \in \mathcal{A}(x_1) \cap \mathcal{A}(x_2)} \rho(a_i^\top x + b_i) \leq \sum_{i \in \mathcal{A}(x_1) \cap \mathcal{A}(x_2) \cap \mathcal{A}(x_0)} \rho(a_i^\top x + b_i) + \sum_{i \in \mathcal{A}(x_1) \cap \mathcal{A}(x_2) \cap \mathcal{A}(x_3) \setminus (\mathcal{A}(x_1) \cap \mathcal{A}(x_2) \cap \mathcal{A}(x_0))} \rho(a_i^\top x + b_i).$$

We define

$$f_1(x) := \sum_{i \in \mathcal{A}(x_1) \cap \mathcal{A}(x_2) \cap \mathcal{A}(x_0)} \rho(a_i^\top x + b_i),$$

$$f_2(x) := \sum_{i \in (\mathcal{A}(x_1) \cap \mathcal{A}(x_2) \cap \mathcal{A}(x_3)) \setminus (\mathcal{A}(x_1) \cap \mathcal{A}(x_2) \cap \mathcal{A}(x_0))} \rho(a_i^\top x + b_i).$$

We exemplarily do the discussion for  $f_1$ . Due to  $f_j \geq 0$ ,  $j \in \{1, 2\}$ , (39) and by assumption (38) we know that

$$\epsilon \geq |f_1((-\frac{k}{2}, 0)^\top) - f_1(x_0)| = \left| \sum_{i \in \mathcal{A}(x_1) \cap \mathcal{A}(x_2) \cap \mathcal{A}(x_0)} a_i^\top (-\frac{k}{2}, 0)^\top \right|$$

and, thus,

$$(40) \quad \left| \sum_{i \in \mathcal{A}(x_1) \cap \mathcal{A}(x_2) \cap \mathcal{A}(x_0)} (a_i)_1 \right| \leq \frac{2\epsilon}{k}.$$

Moreover, due to the properties of  $h$  on  $\{-\frac{k}{2}\} \times (-\frac{k}{2}, \frac{k}{2})$  we know that

$$\epsilon \geq |f_1((-\frac{k}{2}, 0)^\top) - f_1((-\frac{k}{2}, \pm \frac{k}{2})^\top)| = \left| \sum_{i \in \mathcal{A}(x_1) \cap \mathcal{A}(x_2) \cap \mathcal{A}(x_0)} a_i^\top (0, \pm \frac{k}{2})^\top \right|$$

and, thus,

$$(41) \quad \left| \sum_{i \in \mathcal{A}(x_1) \cap \mathcal{A}(x_2) \cap \mathcal{A}(x_0)} (a_i)_2 \right| \leq \frac{2\epsilon}{k}.$$

Assumption (38) further yields

$$(42) \quad \epsilon \geq |f_1((0, 0)^\top)| = \left| \sum_{i \in \mathcal{A}(x_1) \cap \mathcal{A}(x_2) \cap \mathcal{A}(x_0)} b_i \right|.$$

Combination of (40), (41) and (42) yields

$$\begin{aligned} |f_1(x)| &= \left| \sum_{i \in \mathcal{A}(x_1) \cap \mathcal{A}(x_2) \cap \mathcal{A}(x_0)} a_i^\top x + b_i \right| \\ &\leq \left\| \sum_{i \in \mathcal{A}(x_1) \cap \mathcal{A}(x_2) \cap \mathcal{A}(x_0)} a_i \right\| \|x\| + \left\| \sum_{i \in \mathcal{A}(x_1) \cap \mathcal{A}(x_2) \cap \mathcal{A}(x_0)} b_i \right\| \\ &\leq \frac{2\sqrt{2}\epsilon}{k} \sqrt{2}k + \epsilon \leq 5\epsilon. \end{aligned}$$

A similar estimate can also be derived for  $f_2$ . Hence, subtracting all  $i \in \mathcal{A}(x_1) \cap \mathcal{A}(x_2)$  just changes the approximation in the order of  $\epsilon$ . Therefore, without loss of generality (by possibly adapting  $\epsilon$ ), we can assume that for  $f_{\theta, \epsilon}$  it holds that  $\mathcal{A}(x_1) \cap \mathcal{A}(x_2) = \emptyset$ .



### A.2.2. Proof by Contradiction.

LEMMA 8. Let  $d \in \mathbb{N}$ ,  $N \in \mathbb{N}$ ,  $\{a_i, b_i\}_{i \in \{1, \dots, N\}}$  be such that  $a_i \in \mathbb{R}^d$ ,  $b_i \in \mathbb{R}$  for all  $i \in \{1, \dots, N\}$ . Let  $f(x) := \sum_{i=1}^N \rho(a_i^\top x + b_i)$  with  $\rho(s) = \text{ReLU}(s)$ . Let  $x_1, x_2 \in \mathbb{R}^d$  be such that  $\mathcal{A}(x_1) \cap \mathcal{A}(x_2) = \emptyset$ , where  $\mathcal{A}(x)$  is defined by (34). Then

$$\tilde{f}(x) := \sum_{j=1}^2 \rho\left(\sum_{i \in \mathcal{A}(x_j)} a_i^\top x + b_i\right)$$

fulfills  $\tilde{f}(x_j) = f(x_j)$  for  $j \in \{1, 2\}$  and  $\tilde{f}(x) \leq f(x)$  for all  $x \in \mathbb{R}^d$ . Moreover,  $\sum_{i \in \mathcal{A}(x_j)} a_i$  is an element of the subdifferential  $\partial f(x_j)$  of  $f$  in  $x_j$ .

*Proof.* Follows with the same arguments as in the proof of Lemma 7.  $\square$

Assume that  $f_\theta$  is a convex function with  $\mathcal{A}(x_1) \cap \mathcal{A}(x_2) = \emptyset$  (can be assumed due to section A.2.1) and such that

$$(43) \quad |f_\theta(x) - h(x)| \leq \epsilon$$

for all  $x \in K$ . Hence, for  $\epsilon > 0$  sufficiently small, there exists a  $C > 0$  independent of  $k$  and  $\epsilon$  such that

$$(44) \quad \begin{aligned} \|g_1 - (1, 1)^\top\| &\leq \frac{C}{k}\epsilon, \\ \|g_2 - (1, -1)^\top\| &\leq \frac{C}{k}\epsilon, \end{aligned}$$

for all  $g_1 \in \partial f_\theta(x_1)$ ,  $g_2 \in \partial f_\theta(x_2)$ , and

$$(45) \quad \left| \sum_{i \in \mathcal{A}(x_j)} b_i \right| \leq C\epsilon$$

for  $j \in \{1, 2\}$ .

Due to the properties of  $\rho$ , for  $a, c \in \mathbb{R}^d$  with  $\|a - c\| \leq \frac{C}{k}\epsilon$  and  $b, d \in \mathbb{R}$  with  $\|b - d\| \leq C\epsilon$ , there exists a constant  $\tilde{C} > 0$  such that

$$\|\rho(a^\top x + b) - \rho(c^\top x + d)\| \leq \tilde{C}\epsilon$$

for all  $x \in K$ . Hence, with (44) and (45),

$$(46) \quad \|f_\theta(x) - (\rho((1, 1)^\top x) + \rho((1, -1)^\top x))\| \leq \tilde{C}\epsilon.$$

Combining statements (43) and (46) yields a constant  $\hat{C} > 0$  such that

$$(47) \quad \|(\rho((1, 1)^\top x) + \rho((1, -1)^\top x)) - h(x)\| \leq \hat{C}\epsilon.$$

However, for  $x_\alpha = (\alpha, 0)^\top$ , it holds that

$$(48) \quad \|(\rho((1, 1)^\top x_\alpha) + \rho((1, -1)^\top x_\alpha)) - h(x_\alpha)\| = \alpha$$

for all  $\alpha \in (0, k)$ . Hence, for  $\epsilon$  sufficiently small or  $k$  sufficiently big, this yields a contradiction.